Feynman diagrammatics based on discrete pole representations: A path to renormalized perturbation theories

Daria Gazizova,[1] Lei Zhang [orcid],[2] Emanuel Gull [orcid],[2] and J. P. F. LeBlanc [orcid][1,*]

[1]*Department of Physics and Physical Oceanography, Memorial University of Newfoundland,*
St. John's, Newfoundland and Labrador, Canada A1B 3X7
[2]*Department of Physics, University of Michigan, Ann Arbor, Michigan 48109, USA*

By merging algorithmic Matsubara integration with discrete pole representations we present a procedure to generate fully analytic closed form results for impurity problems at fixed perturbation order. To demonstrate the utility of this approach we study the Bethe lattice and evaluate the second-order self-energy for which reliable benchmarks exist. We show that, when evaluating diagrams on the Matsubara axis, the analytic sums of pole representations are extremely precise. We point out the absence of a numerical sign problem in the evaluation, and explore the application of the same procedure for real-frequency evaluation of diagrams. We find that real-frequency results are subject to noise that is controlled at low temperatures and can be mitigated at additional computational expense. We further demonstrate the utility of this approach by evaluating dynamical mean field and bold diagrammatic self-consistency schemes at both second and fourth order and compare to benchmarks where available.

I. INTRODUCTION

The Matsubara formalism for Feynman diagrammatics is a cornerstone of computational condensed matter physics that appears throughout the literature on finite temperature methods for computing many-body systems. The vast majority of applications use only the lowest-order diagrams such as those for polarization, random-phase approximation, *GW*, and the second-order self-energy. These key low-order diagrams find application in a wide range of quantum chemistry and materials physics problems. Not surprisingly there are many problems for which low-order diagrams are insufficient and this leads to renormalized perturbative approaches and self-consistent schemes in an attempt to capture essential features of higher-order diagrams [1–10].

Moving beyond low orders is rarely straightforward. However, in the case of noninteracting problems recent advancements allow one to automatically evaluate internal temporal integrals using algorithmic Matsubara integration (AMI) [11] which produces expressions analogous to those typically used at low orders and has been applied to compute a variety of properties of the Hubbard model [12–17] as well as the real-frequency response functions needed to obtain the correlation exchange kernel in the jellium model [18–21]. Using AMI relies on contour integration methods to evaluate nested Matsubara sums and therefore hinges on having access to the analytic pole structure of a diagram's constituents which typically means that the states (or bands) have known analytic form or energies that can be represented in a diagonal basis [22,23]. This prevents the method from being used for iterative or self-consistent calculations in most cases. One

path around this is to use a full spectral decomposition of a diagram for which the internal integration space grows and becomes quickly intractable as order increases, again limiting evaluation to low-order diagrams [19].

In this paper we explore the use of pole decompositions on Matsubara axis Green's functions and test their utility for evaluating convolutions of Green's functions that arise in Feynman diagrams. Using the semicircular density of states as the simplest possible test case we invoke discrete pole decompositions of the Matsubara axis Green's function: the discrete Lehmann representation (DLR) and the Prony representation [24,25]. We then evaluate the second-order self-energy using the full spectral representation as well as derive an analogous expression for the self-energy based on either pole decomposition. We find that results for the self-energy employing a discrete pole representation are extremely stable and accurate on the Matsubara axis and can be obtained at a small fraction of the computational expense when compared to the full spectral representation. We show how the method can be applied iteratively for data on the Matsubara axis and show that the converged result can be directly evaluated near the real-frequency axis with a finite regulator. We find that doing so suffers from oscillatory errors due to discretization and suggest methods of mitigating this issue. Finally, we show the method can be extended to arbitrary orders, demonstrate a self-consistency loop performed at fourth order, and highlight differences from lower-order self-consistency.

II. METHODS

A. Standard spectral representation

Feynman diagrams are composed of products of Green's functions with arguments both internal and external to the diagram. For simplicity, we will restrict discussion to

a self-energy diagrammatic expansion at order m. Each mth-order diagram must be summed over m independent internal Matsubara frequencies, $\{i\nu_i\} = (i\nu_1, \ldots, i\nu_m)$, but contains a product of $2m - 1$ Green's functions, m of which have independent labels in $\{i\nu_i\}$, and the remaining $m - 1$ have dependent labels that are some linear combination of $\{i\nu_i\}$ as well as an external Matsubara frequency, $i\nu_x$. We annotate such a linear combination as $\vec{\alpha} \cdot \vec{v}$ where $\vec{v} = (i\nu_1, \ldots, i\nu_m, i\nu_x)$ and $\vec{\alpha}$ is a vector of the same length representing coefficients with values ± 1 or 0.

An arbitrary self-energy diagram will take the form

$$\Sigma(i\nu_x) = \sum_{\{i\nu_i\}} H(\{i\nu_i\}, i\nu_x) \qquad (1)$$

where $H(\{i\nu_i\}, i\nu_x)$ is a product of Green's functions given by

$$H(\{i\nu_i\}, i\nu_x) = G(i\nu_1) \ldots G(i\nu_m) G(\vec{\alpha}_1 \cdot \vec{v}) \ldots G(\vec{\alpha}_{m-1} \cdot \vec{v}). \qquad (2)$$

After a Matsubara sum is performed each term will also be in the form of Eq. (2) allowing the Matsubara sums to be performed in sequence.

The spectral representation for a single Green's function is an integral representation given by

$$G(i\nu_n) = \int_{-\infty}^{\infty} \frac{A(x)}{i\nu_n - x} dx, \qquad (3)$$

where the spectral density, $A(x)$, is a function of a real frequency, x, and in the case of causal functions is related to the imaginary part of the Green's function on the real-frequency axis. One can then apply the spectral representation of Eq. (3) to each Green's function in Eq. (2) and this is the typical spectral representation of a Feynman diagram which, dropping overall prefactors and interaction terms, would appear in the form

$$\Sigma(i\nu_x) = \sum_{\{i\nu_i\}} \iint A(x_1) \ldots A(x_{2m-1}) \qquad (4)$$

$$\times \prod_{\ell=1}^{m} \frac{1}{i\nu_\ell - x_\ell} \prod_{j=1}^{m-1} \frac{1}{\vec{\alpha}_j \cdot \vec{v} - x_{j+m}} dx_1 \ldots dx_{2m-1}. \qquad (5)$$

This is useful because the order of Matsubara integration and spectral integration can be interchanged, and the Matsubara sums can be performed analytically since the product of kernels is identical to a product of noninteracting Green's functions. The Matsubara sums for any such diagram can be symbolically generated via AMI for which computational tools exist [11,26,27]. The result of those summations will be in the form

$$\Sigma(i\nu_x) = \iint A(x_1) \ldots A(x_{2m-1})$$
$$\times I(\beta, \{x_i\}, i\nu_x) dx_1 \ldots dx_{2m-1} \qquad (6)$$

where $I(\beta, \{x_i\}, i\nu_x)$ is given by

$$I(\beta, \{x_i\}, i\nu_x) = \sum_{\text{terms}} F(\beta, \{x_i\}) \prod G_0(i\nu_x, \{x_i\}). \qquad (7)$$

Here $F(\beta, \{x_i\})$ is an analytic function containing sums and products of Fermi and Bose distribution functions and their

derivatives, G_0 are noninteracting Green's functions arising from the kernel of the spectral representation, and the sum is over terms that typically factorize at intermediate steps in the Matsubara summation. The form of $I(\beta, \{x_i\}, i\nu_x)$ will be distinct for each diagram topology but can be automatically generated by the AMI procedure [26,27].

This general spectral representation can be used for any choice of spectral density, and so is not restricted to noninteracting problems while the Matsubara sums are still trivially constructed using AMI or, in the case of Green's function expansions, via other direct analytic approaches [28]. Most importantly, the analytic continuation of the external frequency $i\nu_x \to \omega + i0^+$ is allowed after Matsubara sums are performed. However, the limitations of this approach are severe. One has added to the original problem of summing m independent Matsubara frequencies a new set of $(2m - 1)$ nested integrals with infinite bounds. In many cases the product of spectral functions is very sparse, leading to a numerical sign (phase) problem when using stochastic methods that typically worsens as order increases. For that reason, this is typically only done for lowest-order diagrams such as a particle-hole bubble, $\Pi = GG$, or the GW approximation, $\Sigma = GW$, since the number of spectral integrals in these cases is only two, and these can be further reduced to just two one-dimensional integrals. Finally, the form of Eq. (7) holds and can be analytically continued for two-point correlation functions where there is a single external frequency. In the case of multipoint correlators there are multiple Matsubara frequencies that need to be analytically continued and this complication is nontrivial to resolve [29,30].

B. Discrete pole representations

1. Discrete Lehmann representation

The DLR [24,31,32] is a pole representation [33–37] for functions that have a spectral decomposition that can be well approximated in a truncated form

$$G(i\omega_n) = \int_{-\Lambda}^{\Lambda} K(i\omega_n, x)\rho(x) dx, \qquad (8)$$

where ρ is the density and the kernel is given by $K(i\omega_n, x) = \frac{1}{i\omega_n - x}$ when represented in Matsubara frequencies. The formulation of DLR in the frequency domain assigns a set of frequencies along the imaginary axis, $\{i\omega_{\text{DLR}}\}$, that are determined uniquely for a given choice of Λ and an error tolerance at a temperature β to ensure that the kernel is well approximated in the domain $[-\Lambda, \Lambda]$ based on a discrete set of poles along the real axis, $\{\omega_k\}$. If this can be accomplished then the Green's function can be approximated as a sum over a finite set of poles $\{\omega_k\}$ with weights g_k as

$$G(i\omega_n) \approx G_{\text{DLR}}(i\omega_n) = \sum_{k=1}^{r} K(i\omega_n, \omega_k) g_k. \qquad (9)$$

In essence the intent is to leverage the flexibility in defining $\rho(x)$ in Eq. (8) and is equivalent to assuming

$$\rho(x) = \sum_{k=1}^{r} g_k \delta(x - \omega_k). \qquad (10)$$

In the limits of both $r, \Lambda \to \infty$, the weights should be continuous and if $g_k \to A(\omega_k)$ then the normal spectral representation is recovered.

2. Prony approximation

The Prony approximation [25] results in a pole decomposition of the form

$$G_P(z) = \sum_{k=1}^{r} \frac{g_k}{z - \omega_k}. \tag{11}$$

The fit to the function is generated by first mapping an interval of the non-negative imaginary axis to a unit circle. The Prony approximation then generates a set of poles and weights to satisfy $G(i\omega_n)$. There are two variants of the Prony approximation we will discuss. The first, which we call Prony analytic continuation (PRONYAC), is the Prony representation as presented in Ref. [25] (see also Refs. [38,39]) that can be used on discrete data for $G(i\omega_n)$ as a form of analytic continuation to the real-frequency axis. The PRONYAC method generates a set of complex poles ω_k in the lower-half plane with complex weights g_k. The resulting function is valid for arguments z in the entire upper-half plane *and* along the real axis. In this paper we use PRONYAC as a form of numerical analytic continuation which for sufficiently high-quality data on the Matsubara axis should provide a causal analytic continuation.

For the purposes of evaluating Feynman diagrams, the function generated by PRONYAC is not straightforward to implement, since the function generated by PRONYAC only approximates the retarded Green's function in the upper half of the complex plane but does not approximate the advanced Green's function in the lower half of the complex plane. In this paper, we modify the holomorphic mapping in the Prony formalism to generate a symmetrized function valid in both the upper- and lower-half planes resulting in a function with poles that are real, as well as pairs of complex poles that are complex conjugates. This introduces poles directly on the real axis, similar to DLR. Nevertheless, the Prony approximation generates a minimal pole representation of the symmetrized function that can then be employed interchangeably with DLR since they are valid in both upper- and lower-half planes. For the purposes of performing Matsubara sums, we will use this second form of the Prony approximation, and approximate the Green's function on the Matsubara axis with $G(i\omega_n) \approx G_P(i\omega_n)$.

3. Analytic continuation of diagrams involving pole representations

Above we have introduced notation for the DLR and the symmetrized Prony Green's functions, G_{DLR} and G_P respectively. Much of the discussion in the following sections pertains to either representation. We will use G_D to represent either discrete pole representation. Given a single-particle Green's function on the Matsubara axis, the density is related to the imaginary part of the analytic continuation of the Green's function, $\rho(\omega) = -\frac{1}{\pi}\text{Im}G(i\omega \to \omega + i0^+)$. It is straightforward to see from the discrete nature of the pole representations that we cannot analytically continue the discretized G_D and have any hope of reconstructing the original continuous function on the real-frequency axis. This is not

surprising since no information regarding the function on the real-frequency axis is required to generate a pole representation. It is therefore the case that $G(\omega + i0^+) \neq G_D(\omega + i0^+)$ for any finite number of poles.

However, when evaluating the analytic continuation in practice one includes a finite regulator $i\omega_n \to \omega + i\Gamma$ which should produce a sufficiently accurate result for a sufficiently small choice of Γ. We therefore expect that $G(\omega + i\Gamma) = G_D(\omega + i\Gamma)$ for a sufficiently large Γ, and given the constraint along the imaginary axis that $G(i\omega_0) = G_D(i\omega_0)$ (to a controllable precision) we are guaranteed that the pole representation will produce the correct function at low energies for $\Gamma \approx \pi/\beta$. Therefore, as temperature decreases towards zero Γ can be made arbitrarily small. In the case of a discrete representation of a single Green's function on the Matsubara axis, one would not analytically continue using DLR or the symmetrized Prony Green's functions. These are by construction not well behaved on the real axis. Instead other methods are preferable such as NEVANLINNA [40–42] or the above mentioned PRONYAC [25].

In what follows we are interested in using pole representations to evaluate sums over products of G_D Green's functions. The above arguments lead us to expect that such diagram evaluations can be analytically continued directly so long as a sufficiently large regulator is employed, where size is defined by the scale of π/β.

4. Matsubara sums of products of G_D

When given a Green's function, or product thereof, on the Matsubara axis with a set of known poles, the Matsubara sums can be performed analytically via contour integration. For example, to treat the sum over a particular function $H(i\omega_n)$, assumed to be a product of single-particle Matsubara Green's functions defined in both the upper-half and lower-half planes, one solves the auxiliary problem of integrating $H(z)$ multiplied by a Fermi or Bose function to match the statistics of $i\omega_n$. This is then integrated along two contours; $C1$, along the real axis closed in the upper-half plane, and $C2$, along the real axis in the negative direction and closed in the lower-half plane. These contours enclose the poles of the Fermi or Bose functions [$f(z)$ and $n(z)$ respectively] which are the set of Matsubara frequencies $\{i\omega_n\}$ as well as the set of poles, $\{z_0\}$, of $H(z)$. In the case of fermions, the sum of $C1$ and $C2$ gives

$$\oint_{C1+C2} f(z)H(z)dz = 0 = -\frac{1}{\beta}\sum_{i\omega_n} H(i\omega_n) + \sum_{\{z_0\}} \text{Res}[f(z)H(z)]_{z_0}. \tag{12}$$

We see right away that the value of $H(z)$ as a continuous function on the real axis does not appear in the right-hand equality, and only the poles of $H(z)$ contribute. It is tempting therefore to replace the representation of $H(i\omega_n)$ with a discrete pole representation,

$$\sum_{i\omega_n} H(i\omega_n) \approx \sum_{i\omega_n} H_D(i\omega_n), \tag{13}$$

where for a sufficiently high precision representation of the Green's function we presume that H_D is given by an

appropriate product of G_D Green's functions. Since Eq. (12) holds for both $H(z)$ and $H_D(z)$ one can approximate the original Matsubara sum:

$$\frac{1}{\beta} \sum_{i\omega_n} H(i\omega_n) \approx \sum_{\{\omega_k\}} \text{Res}[f(z)H_D(z)]_{\omega_k}. \quad (14)$$

A similar relation holds for bosonic frequency summation with replacement of $f(z) \to -n(z)$.

This simple relationship allows for the systematic sequential evaluation of a series of nested Matsubara sums over frequencies $i\nu_i$ where each has poles given by the sets $\{\omega_{k_i}\}$ as needed in Eq. (1). Each k_i runs a range of values from $1 \to r_i$ as in Eqs. (9) and (11). This gives a result analogous to Eq. (6):

$$\Sigma(i\nu_x) \approx \sum_{k_1, k_2, \ldots, k_{2m-1}} g_{k_1} \cdots g_{k_{2m-1}}$$
$$\times F(\beta, \{\omega_{k_i}\}) \prod G_0(i\nu_x, \{\omega_{k_i}\}). \quad (15)$$

We see from this expression that there is a one-to-one correspondence between the discrete spectral amplitudes, g_{k_i}, and the standard spectral functions, $A(x_i)$, in Eq. 6. The auxiliary integrations over the continuous valued set of real frequencies $\{x_i\}$ are now discrete summations over the poles $\{\omega_{k_i}\}$. It is important to note that the G_0 functions that appear in Eq. (15) do not arise from the discretization of the density $\rho(x)$ but are actually the kernel of Eq. (8) and therefore have a well-defined analytic continuation such that $i\nu_x$ in Eq. (15) can be safely analytically continued to the real-frequency axis.

If this representation of Matsubara sums is accurate for a manageable number of poles then the reduction in complexity for renormalized perturbative problems is enormous even at low orders. There are two key advantages. First, it replaces the arbitrary sampling of each integration axis with a fixed scaling of $(r)^{2m-1}$. Second, when performing iterative calculations it bypasses the evaluation of a real-frequency axis density, $\rho(x)$, a process that requires generating a dense grid of real frequencies in order to resolve the salient features of a possibly unknown function. Instead one only needs to evaluate the self-energy along the Matsubara axis in order to generate a next approximation of $G(\{i\omega_{\text{DLR}}\})$ or at an appropriate set of Matsubara points in the upper-half plane for the Prony approximation.

All of this advantage, however, hinges delicately on the accuracy of Eq. (15) which cannot be clearly estimated based on accuracy constraints of a DLR or Prony fit.

C. Test case

In what follows we test our approach on a Bethe lattice, an impuritylike problem with no momentum dependence, and a semicircular density of states for which there is a known analytic solution. The semicircular density of states is given by $A(\omega) = \frac{1}{2\pi t^2}\sqrt{4t^2 - \omega^2}$ and the Matsubara Green's function in the upper-half plane is given by $G(i\omega_n) = \frac{i}{2t^2}(\omega_n - \sqrt{\omega_n^2 + 4t^2})$. In this representation the bandwidth is $4t$ and we operate in units of $t = 1$.

III. RESULTS

A. Matsubara-frequency axis

We first explore evaluation of the self-energy on the Matsubara axis. As a starting point, using the semicircular density of states we compute the second-order self-energy using the full spectral representation of Eq. 6, $\Sigma_{\text{spec}}^{(2)}(i\nu_x)$ for which the Matsubara sums can be performed by hand. In the case of DLR, we generate for the semicircular density of states the Green's function at $\{i\omega_{\text{DLR}}\}$ from which the poles, $\{\omega_k\}$, and weights, g_k, are determined using LIBDLR [31]. In the case of Prony, we generate for the semicircular density of states the Green's function at a finite set of Matsubara points in the upper-half plane $\{i\omega_n\}$ from which the poles, $\{\omega_k\}$, and weights, g_k, are determined using PRONYAC, part of the GREEN package [25,43–45].

The second-order contribution in the full spectral representation is given by

$$\Sigma_{\text{spec}}^{(2)}(i\nu_x)$$
$$= \iiint A(x_1)A(x_2)A(x_3)$$
$$\times \frac{[f(x_1) - f(x_2)][n(x_2 - x_1) + f(-x_3)]}{i\nu_x + x_1 - x_2 - x_3}dx_1 dx_2 dx_3, \quad (16)$$

where $f(x)$ and $n(x)$ are Fermi and Bose distribution functions respectively. The analogous expression making use of the G_D Green's functions is

$$\Sigma_D(i\nu_x) = \sum_{k_1, k_2, k_3} g_{k_1} g_{k_2} g_{k_3}$$
$$\times \frac{[f(\omega_{k_1}) - f(\omega_{k_2})][n(\omega_{k_2} - \omega_{k_1}) + f(-\omega_{k_3})]}{i\nu_x + \omega_{k_1} - \omega_{k_2} - \omega_{k_3}}. \quad (17)$$

Both Σ_{spec} and Σ_D are presented here assuming only simple poles. In both cases when poles coincide the expressions produce removable divergences and can be treated properly using AMI. For brevity we forego these details.

For comparison, we evaluate Σ_D and Σ_{spec} and plot the imaginary parts in Figs. 1(a) and 1(b) for $\beta = 5$ and 20 respectively. The analytic sums Σ_{DLR} and Σ_P are visually identical to the integral of the spectral representation for all Matsubara points. This result is extremely stable to variation in the discrete pole representation, and we scrutinize the accuracy of the comparison in Fig. 1(c). We plot the absolute deviation of DLR and Prony pole representations from the benchmark spectral result, $\Delta\Sigma = |\Sigma_D - \Sigma_{\text{spec}}|$, as a function of the number of poles, r, for the zeroth Matsubara frequency. We also show the deviation $\Delta\Sigma = |\Sigma_{\text{DLR}} - \Sigma_P|$ to illustrate the behavior of the pole representations relative to each other. We see that with respect to the Σ_{spec} benchmark both the DLR and Prony representations converge to the same result, with a deviation within the error estimate of the benchmark, 1×10^{-7}. This suggests that both methods are converging to a correct physical value. One sees that the deviation between the two pole methods does not plateau and that continued increase in the accuracy of the pole representation gives agreement with the two approaches on the scale of 1×10^{-9} by $r = 21$. We
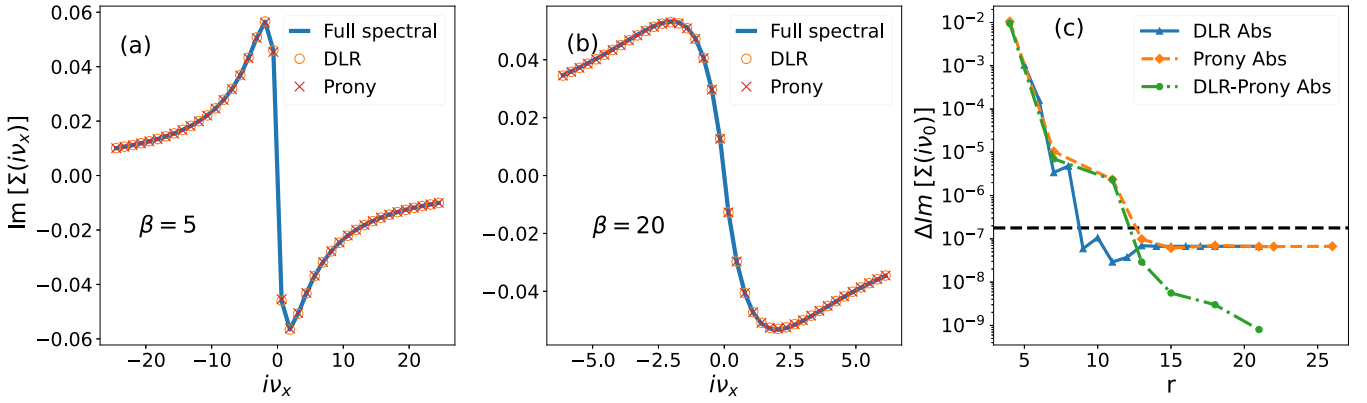
FIG. 1. Imaginary part of self-energy in Matsubara frequencies $i\nu_x$ for the full spectral, DLR, and Prony representations. (a) $\beta = 5$. (b) $\beta = 20$. (c) Absolute difference for $i\nu_0$ at $\beta = 5$. Horizontal dashed line represents the uncertainty estimate of Σ_{spec}.

believe this represents an essentially exact numerical result, that is also the physically correct value. It is worth noting the difference in computational expense between Eq. (6) for $\Sigma_{\text{spec}}^{(2)}$ and Eq. (15) for the pole representations. Both have nearly identical analytic form and therefore similar computational expense per evaluation of the integrand/summand. Without prior knowledge of $A(x_i)$ the computational expense of the three nested integrals in $\Sigma_{\text{spec}}^{(2)}$ is extremely large. Our estimate of $\Sigma_{\text{spec}}^{(2)}(i\nu_0)$ in Fig. 1(c) was evaluated to an absolute accuracy of 2×10^{-7} and required on the order of 10^7 function evaluations. In contrast the pole representations require precisely r^3 evaluations. We see that even for a small number of poles the DLR and Prony results are extremely accurate. At $r = 5$ the DLR result is accurate within 2% of the spectral result while only requiring $5^3 = 125$ function evaluations. This improves exponentially such that by $r = 8$ the relative difference is 1×10^{-6} for $8^3 = 512$ evaluations.

Even for only a second-order self-energy, this computational advantage is enormous and will grow exponentially as the diagram order increases. The pole representations have shifted the spectral integration weight to a finite and *known* set of $\{\omega_k\}$ poles. This is in contrast to high-order integration of continuous functions where an integration routine needs to search for where the integrand has value. Doing so one encounters sampling issues such as a numerical sign problem. This is not the case here, where one simply evaluates a discrete set of predetermined points where all the weight has been placed. There is no longer a sign problem because there is no stochastic component or variance. While there remains an exponential expense in the number of poles we foresee opportunities for approximations of the pole representations where one removes poles with small g_k values, but note that such exclusions should be performed with care since in principle their impact would be uncontrolled.

We note that there exist sparse methods for evaluating discrete Matsubara sums [34,46]. If applied to this second-order problem on the Matsubara axis those approaches will exhibit similar scaling dependent upon the size of the basis used.

B. Real-frequency axis

Turning to real frequencies, we evaluate $\text{Im}\Sigma_{\text{spec}}^{(2)}$ and $\text{Im}\Sigma_{D}^{(2)}$ replacing the external frequency $i\nu_x \rightarrow \omega + i\Gamma$ and

present results for a choice of $\Gamma = 0.1$ for $\beta = 5$ and 20 in the first and second rows of Fig. 2 respectively. One notes that the Prony and DLR results oscillate around the benchmark from the full spectral case. These oscillations have a number of origins, including overfitting, but are largely due to the fact that G_D is not the physical function on the real axis, but has been discretized, and the oscillations originate from the spacing of the real-frequency poles.

We see from the left-hand column of Fig. 2 that for a fixed choice of the regulator Γ the region at small ω for $\beta = 5$ has severe oscillations and that these are dampened by decreasing temperature to $\beta = 20$. In the case of DLR, we see that the oscillations that are absent at low frequency return at higher frequency. In the case of the Prony approximation the result is well behaved both at low and high frequencies and exhibits oscillatory behavior at intermediate points. Importantly, in all cases we find that these oscillations are not fundamental to the evaluation, meaning that distinct pole representations will find distinct oscillatory patterns, and therefore these oscillations can be mitigated in a number of ways. First, we can generate the self-energy for a variety of slightly different DLR/Prony fits, and use the average of the result to suppress the
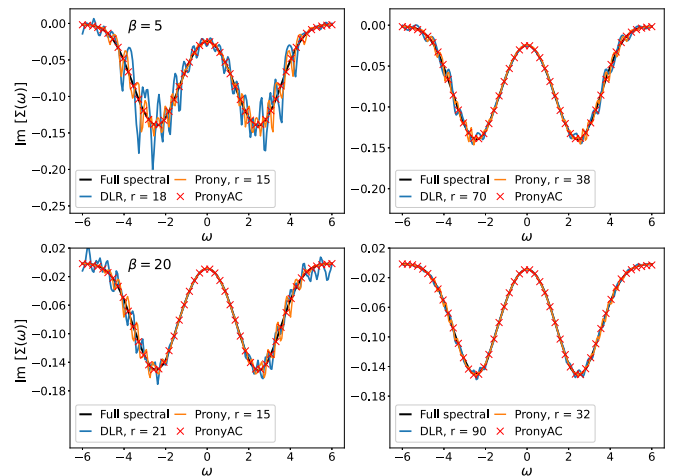

FIG. 2. Imaginary part of self-energy for frequency $i\omega_n \rightarrow \omega + i\Gamma$ for $\beta = 5$ and 20 using spectral, DLR, and Prony representations. Analytic continuation is performed using $\Gamma = 0.1$.
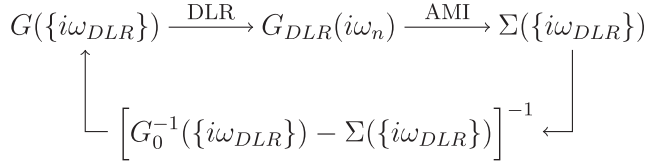
$$G(\{i\omega_{DLR}\}) \xrightarrow{\text{DLR}} G_{DLR}(i\omega_n) \xrightarrow{\text{AMI}} \Sigma(\{i\omega_{DLR}\})$$

$$\left[G_0^{-1}(\{i\omega_{DLR}\}) - \Sigma(\{i\omega_{DLR}\}) \right]^{-1} \leftarrow$$

FIG. 3. Iterative scheme for perturbative calculation.

oscillations. A second approach is to artificially increase the basis size r by creating a new pole representation as an average over two or more fits. This increases the number of poles and allows us to generate finer grids.

We do the latter in the right-hand column of Fig. 2. At fixed Γ and β we merge a number of DLR/Prony representations of G_D to generate a larger basis and use this to perform the same calculation. In each case we see strong reduction in oscillations on the real-frequency axis. Finding an optimal way to accomplish this would be an important contribution in the future. To summarize, results in real frequency are more sensitive to the details of the pole representation, but appear controllable by increasing the number of DLR/Prony nodes.

What is truly desired is analytic continuation in the $\Gamma \to 0^+$ limit, which the above approach cannot accomplish, though it remains a useful approach to check other forms of numerical analytic continuation. We illustrate also in Fig. 2 the analytic continuation of PRONYAC with the same regulator, which very accurately reproduces the benchmark spectral result with no spurious oscillations. The causal nature of PRONYAC makes it a powerful numerical analytic continuation tool when combined with the high precision Matsubara axis data generated using our AMI toolset.

C. Self-consistent calculations

There are two obvious paths forward using the pole representations for self-consistent calculations. The first is self-consistent perturbation theory, or bold diagrammatics, which we can evaluate to any order but here restrict to second order. This is therefore equivalent to the well-known GF2 method. The second is dynamical mean field theory (DMFT) using the second-order diagram as a solver. These calculations can be done using either DLR or the Prony representations. Since both are controlled and produce virtually identical results on the Matsubara axis we present in this section results using the DLR where we leverage the sparseness of the DLR representation that only requires measurement of r points along the imaginary axis $\{i\omega_{DLR}\}$.

1. Self-consistent GF2

Given a Green's function at the DLR Matsubara points $\{i\omega_{DLR}\}$ we find the DLR representation of the Green's function that is a good estimate at all Matsubara points. We can then evaluate a self-energy directly at the points needed $\{i\omega_{DLR}\}$ and using the Dyson equation get a new estimate which can then be used to iteratively compute the next estimate of the self-energy. This iterative scheme is depicted in Fig. 3. We perform the self-consistent perturbation theory for second order using the DLR representation and plot the converged results in Fig. 4 for $\beta = 5$ and 20 assuming a Hubbard
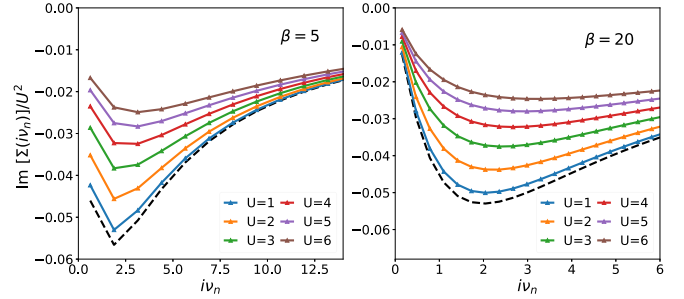

FIG. 4. Imaginary part of the GF2 self-energy in Matsubara frequencies iv_n after self-consistency procedure for different U values. Left, $\beta = 5$; right, $\beta = 20$. DLR representation used $r \approx 25$ for $\beta = 5$ and $r \approx 40$ for $\beta = 20$.

interaction in the range of $U/t = 1 \to 6$ which we suppress in the final result to plot on the same scale. The overall behavior of iterative perturbative methods at low orders typically biases the system towards having a metallic characteristic, indicated by the relative difference of the first two Matsubara frequencies [47,48]. Results appear behaved and insensitive to the detailed choice of the DLR representation.

2. DMFT self-consistency

Here we explore the use of the DLR representation as a diagrammatic solver for DMFT where benchmark results are readily available. The self-consistency loop is that of Fig. 3 except that in each iteration the Green's function must be replaced with a Weiss field in the form $\mathscr{G}(i\omega_{DLR}) = i\omega_{DLR} + \mu - t^2 G_{\text{imp}}(i\omega_{DLR})$ [49,50]. We then find the DLR representation of $\mathscr{G}$ and use this for the next step of the diagrammatic expansion as depicted in Fig. 5.

We compute this first using the DLR representation which requires only the set of $\{i\omega_{DLR}\}$ and then as a benchmark using the standard second-order theory formulated on the imaginary-time axis via the TRIQS package [51]. Results for both are shown in Fig. 6 for $\beta = 5$ and 20, the DLR using solid-colored points, and the DMFT benchmark using open points. Since both are performed to second order they are mathematically equivalent and we find perfect agreement between the methods. There is again a computational advantage at play, as the DLR representation requires substantially fewer evaluations for each iteration replacing continuous integrations with a handful of discrete sums, and in this case does not rely on a Fourier transform from imaginary times. Further, since every DMFT iteration is the evaluation of a closed-form result, there is no stochastic error and we expect our result to be accurate to high precision. We note that one could also use the converged self-energy to do a final iteration of Eq. 15 for which we perform analytic continuation $iv_n \to \omega + i\Gamma$
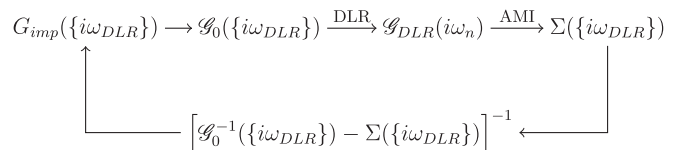
$$G_{imp}(\{i\omega_{DLR}\}) \longrightarrow \mathscr{G}_0(\{i\omega_{DLR}\}) \xrightarrow{\text{DLR}} \mathscr{G}_{DLR}(i\omega_n) \xrightarrow{\text{AMI}} \Sigma(\{i\omega_{DLR}\})$$

$$\left[\mathscr{G}_0^{-1}(\{i\omega_{DLR}\}) - \Sigma(\{i\omega_{DLR}\}) \right]^{-1} \leftarrow$$
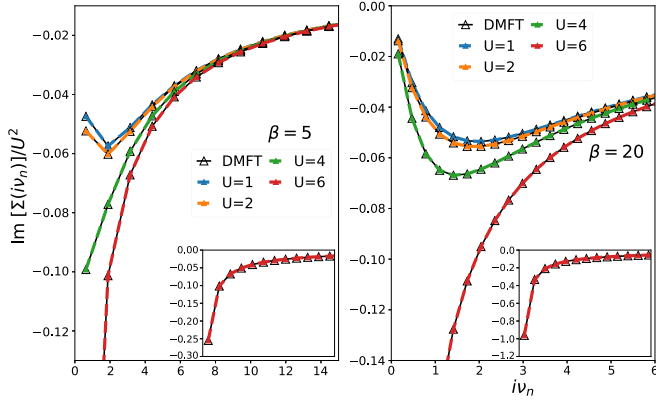
FIG. 5. DMFT self-consistency loop.

FIG. 6. Imaginary part of the converged DMFT self-energy in Matsubara frequencies $i\nu_n$ for different U values. Left, $\beta = 5$ with $r \approx 27$ poles; right, $\beta = 20$ with $r \approx 40$ poles. Comparison DMFT results generated with the TRIQS package [51].

using either the DLR or Prony pole representation. A preferred alternative is to leverage the extreme precision of the DLR+AMI approach on the Matsubara axis to constrain other forms of numerical analytic continuation, such as PRONYAC. Nevertheless, a direct evaluation remains possible as a means of verifying numerical analytic continuation.

D. Beyond second order

Up to this point we have rigorously shown the utility of pole representations for producing analytic closed form results for second-order self-energies, where reliable benchmarks exist, while asserting that this can be used for any diagrammatic expansion. To support this claim, we repeat the self-energy calculations up to fourth order. This involves evaluating two third-order diagrams, the sum of which is zero for particle-hole symmetric problems such as this, as well as 12 fourth-order diagrams. Of the 12 fourth-order diagrams, three include self-energy insertions, leaving nine skeleton diagrams that would be evaluated if doing self-consistency as in Fig. 3. The DMFT self-consistency would require all 12 fourth-order diagrams. We present results at $U = 4$ and $\beta = 5$ for the imaginary parts of the second-, third-, and fourth-order skeleton series after a single iteration in Fig. 7. These parameters were selected since the fourth order is comparable in
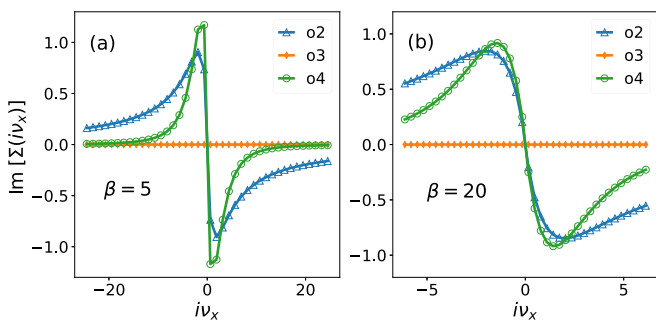

FIG. 7. Imaginary part of skeleton self-energy at orders $2 \rightarrow 4$ in Matsubara frequencies $i\nu_x$ using a DLR representation for $r = 14$ at $U = 4$. (a) $\beta = 5$. (b) $\beta = 20$.
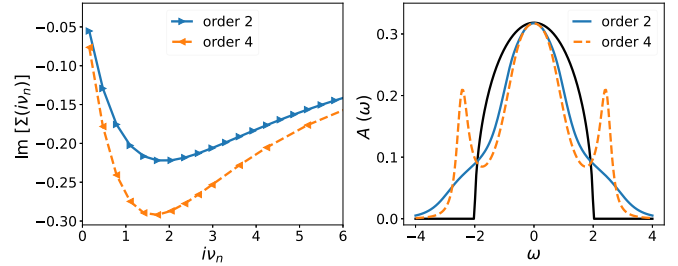

FIG. 8. Left: Imaginary part of the converged DMFT self-energy in Matsubara frequencies $i\nu_n$ generated using DLR representation at $\beta = 20$ and $U = 2$. Right: Spectral function $A(\omega)$ using PRONYAC.

amplitude to the second order. An important check, we see that we recover to high precision the zero contribution from the two third-order diagrams, the sum of which returns values on the scale of 1×10^{-6}. Interestingly, the DLR imposed here does not necessitate more poles as order increases and similar to data for second order in Fig. 1 we find that the result for the imaginary part of $\Sigma^{(4)}(i\omega_0)$ converges by $r = 14$. The reason for this is straightforward. The pole representation assigns an accuracy target to the single-particle Green's function, and increasing the accuracy requires more poles and also finer resolution of the pole amplitudes. While it is true that many poles with weights on the order of 1×10^{-5} are required for high accuracy in the Green's function, since fourth-order diagrams include convolutions of seven Green's functions, poles with such small amplitude become irrelevant, and only a small number of heavy weight poles are needed to accurately reflect the higher-order diagrams.

With this in mind we perform self-consistency within the DMFT framework including self-energies up to fourth order that are iterated to convergence. We present these in the left-hand frame of Fig. 8 contrasted to the earlier result at second order. Here we have chosen the weak coupling case of $U = 2$ and $\beta = 20$. We see that the corrections at fourth order are not small. While the two curves are qualitatively similar, one should recall that small changes on the Matsubara axis can have substantial impact on real-frequency properties. To illustrate this, we contrast the real axis results in the Fig. 8 right-hand frame for the noninteracting, second-order DMFT, and fourth-order DMFT solutions. These curves represent the analytic continuation with no numerical regulator, $\Gamma = 0^+$, enabled by PRONYAC. We see that while low frequency features of $A(\omega)$ are the same, near the band edge, what was a shoulder at second order is now a peak at fourth order, a hallmark feature of metal-insulator transitions.

We note that single-shot self-energy calculations at fourth order have been performed in the past. For example, Ref. [52] laboriously derives integral expressions for the fourth-order diagrams which, for particle-hole symmetric problems, collapse from 12 diagrams to four unique sets of three diagrams [53,54]. They extract the imaginary contributions to $\Sigma^{(4)}$ using a partial spectral representation, leaving a dozen or more integrals to be performed. In our case, we automatically generate the necessary closed-form analytic expressions using AMI, allowing us to evaluate both the real and imaginary parts simultaneously as well as perform self-consistency at minimal computational expense while not being restricted

to particle-hole symmetric problems. We note that other approaches involving the DLR representation merged with the hybridization expansion show promising results as well [55] and have introduced additional simplification that could be adapted to the context of this paper.

IV. CONCLUSIONS

We have outlined a path to performing renormalized diagrammatic calculations by generating a pole representation of the Green's function. We compute GF2 and DMFT self-consistencies for the Bethe lattice using the discrete Lehmann representation combined with algorithmic Matsubara integration. Results are well behaved and essentially exact on the Matsubara axis. We also demonstrate that the result can be analytically continued to the real-frequency axis We have combined this approach with algorithmic Matsubara integration, which allows us to evaluate any diagram using either a DLR or Prony representation. To demonstrate this we evaluate the bold diagrammatic resummation up to fourth order at each iteration (one might call this GF4). Our results represent an exact and purely analytic result of the self-consistency with the only error coming from the expansion into a DLR/Prony basis which is controllable and vanishingly small. We foresee many opportunities for extending this paper. In particular, we note that the procedure is not restricted to impurity problems. Alternatively, one can take a converged result on the Matsubara axis from a preferred method such as DMFT (including cluster extensions such as DCA [56,57], dual fermions [58,59], or dynamical vertex approximation [60]), generate a pole representation, and then use the G_D Green's function to evaluate *any* diagrammatic expansion of interest on both the real- and imaginary-frequency axes. This would be particularly impactful for density-density correlation functions and conductivities that cannot be expanded around the noninteracting solution [61,62] and we expect this can also be adapted to problems in quantum chemistry [1,9,22,23,63–66]. More generally, merging pole representations of Green's functions, effective interactions, and vertex functions for evaluating Feynman diagrams would open the doors to a wide array of renormalization procedures that might be tuned to specific problems or applications. We note as well that other approaches for real-frequency evaluation exist, and might yield similarly useful results via pole representations [30,67]. For example, one can merge the DLR representations of bosonic two-point or three-point functions as a tool for collapsing the diagrammatic expansions [32,35,68,69]. We emphasize that Eq. (15) is general and can be applied to any problem while similar expressions for polarization and other low-order diagrams are trivially converted to the pole representation. Finally, we surmise that alternate pole representations might be constructed that do not suffer from discretization issues on the real axis [25] or that use as a constraint smoothness criteria for analytically continued low-order diagrams for a particular choice of Γ. Such a representation would allow for optimal evaluation on the real-frequency axis without the irregularities present in this paper.

ACKNOWLEDGMENTS

[1] C.-N. Yeh, A. Shee, Q. Sun, E. Gull, and D. Zgid, Relativistic self-consistent *gw*: Exact two-component formalism with one-electron approximation for solids, Phys. Rev. B **106**, 085121 (2022).

[2] A. A. Rusakov, S. Iskakov, L. N. Tran, and D. Zgid, Self-energy embedding theory (SEET) for periodic systems, J. Chem. Theory Comput. **15**, 229 (2019).

[3] S. Iskakov, C.-N. Yeh, E. Gull, and D. Zgid, *Ab initio* self-energy embedding for the photoemission spectra of NiO and MnO, Phys. Rev. B **102**, 085105 (2020).

[4] T. N. Lan and D. Zgid, Generalized self-energy embedding theory, J. Phys. Chem. Lett. **8**, 2200 (2017).

[5] P. Koval, D. Foerster, and D. Sánchez-Portal, Fully self-consistent *GW* and quasiparticle self-consistent *GW* for molecules, Phys. Rev. B **89**, 155417 (2014).

[6] M. Grumet, P. Liu, M. Kaltak, J. c. v. Klimeš, and G. Kresse, Beyond the quasiparticle approximation: Fully self-consistent *GW* calculations, Phys. Rev. B **98**, 155143 (2018).

[7] E. Maggio and G. Kresse, Gw vertex corrected calculations for molecular systems, J. Chem. Theory Comput. **13**, 4765 (2017).

[8] F. Caruso, P. Rinke, X. Ren, A. Rubio, and M. Scheffler, Self-consistent *GW*: All-electron implementation with localized basis functions, Phys. Rev. B **88**, 075105 (2013).

[9] O. J. Backhouse, A. Santana-Bonilla, and G. H. Booth, Scalable and predictive spectra of correlated molecules with moment truncated iterated perturbation theory, J. Phys. Chem. Lett. **12**, 7650 (2021).

[10] G. Harsha, V. Abraham, M. Wen, and D. Zgid, Quasiparticle and fully self-consistent GW methods: an unbiased analysis using Gaussian orbitals, arXiv:2406.18077.

[11] A. Taheridehkordi, S. H. Curnoe, and J. P. F. LeBlanc, Algorithmic Matsubara integration for Hubbard-like models, Phys. Rev. B **99**, 035120 (2019).

[12] A. Taheridehkordi, S. H. Curnoe, and J. P. F. LeBlanc, Algorithmic approach to diagrammatic expansions for real-frequency evaluation of susceptibility functions, Phys. Rev. B **102**, 045115 (2020).

[13] B. D. E. McNiven, G. T. Andrews, and J. P. F. LeBlanc, Single particle properties of the two-dimensional Hubbard model for real frequencies at weak coupling: Breakdown of the Dyson series for partial self-energy expansions, Phys. Rev. B **104**, 125114 (2021).

[14] B. D. E. McNiven, H. Terletska, G. T. Andrews, and J. P. F. LeBlanc, One- and two-particle properties of the weakly interacting two-dimensional Hubbard model in proximity to the Van Hove singularity, Phys. Rev. B **106**, 035145 (2022).

[15] R. Farid, M. Grandadam, and J. P. F. LeBlanc, Pairing susceptibility of the two-dimensional Hubbard model in the thermodynamic limit, Phys. Rev. B **107**, 195138 (2023).

[16] D. Gazizova and J. P. F. LeBlanc, Emergent nearest-neighbor attraction in the fully renormalized interactions of the single-band repulsive Hubbard model at weak coupling, Phys. Rev. B **108**, 165149 (2023).

[17] M. D. Burke, M. Grandadam, and J. P. F. LeBlanc, Renormalized perturbation theory for fast evaluation of Feynman diagrams on the real frequency axis, Phys. Rev. B **107**, 115151 (2023).

[18] J. P. F. LeBlanc, K. Chen, K. Haule, N. V. Prokof'ev, and I. S. Tupitsyn, Dynamic response of an electron gas: Towards the exact exchange-correlation kernel, Phys. Rev. Lett. **129**, 246401 (2022).

[19] I. S. Tupitsyn, A. M. Tsvelik, R. M. Konik, and N. V. Prokof'ev, Real-frequency response functions at finite temperature, Phys. Rev. Lett. **127**, 026403 (2021).

[20] I. S. Tupitsyn and N. V. Prokof'ev, Solving the Bethe-Salpeter equation in real frequencies at finite temperature, Phys. Rev. B **109**, 045152 (2024).

[21] J. P. Perdew, A. Ruzsinszky, J. Tao, V. N. Staroverov, G. E. Scuseria, and G. I. Csonka, Prescription for the design and selection of density functional approximations: More constraint satisfaction with fewer fits, J. Chem. Phys. **123**, 062201 (2005).

[22] I. Assi and J. P. F. LeBlanc, Symbolic determinant construction of perturbative expansions, Phys. Rev. B **109**, 125143 (2024).

[23] J. Li, M. Wallerberger, and E. Gull, Diagrammatic Monte Carlo method for impurity models with general interactions and hybridizations, Phys. Rev. Res. **2**, 033211 (2020).

[24] J. Kaye, K. Chen, and O. Parcollet, Discrete Lehmann representation of imaginary time Green's functions, Phys. Rev. B **105**, 235115 (2022).

[25] L. Zhang and E. Gull, Minimal pole representation and controlled analytic continuation of Matsubara response functions, Phys. Rev. B **110**, 035154 (2024).

[26] H. Elazab, B. McNiven, and J. LeBlanc, Libami: Implementation of algorithmic Matsubara integration, Comput. Phys. Commun. **280**, 108469 (2022).

[27] M. D. Burke and J. P. F. LeBlanc, Torchami: Generalized CPU/GPU implementation of algorithmic Matsubara integration, arXiv:2311.17189.

[28] J. Vučičević and M. Ferrero, Real-frequency diagrammatic Monte Carlo at finite temperature, Phys. Rev. B **101**, 075113 (2020).

[29] A. Ge, J. Halbinger, S.-S. B. Lee, J. von Delft, and F. B. Kugler, Analytic continuation of multipoint correlation functions, Ann. Phys. (NY) **536**, 2300504 (2024).

[30] A. Ge, N. Ritz, E. Walter, S. Aguirre, J. von Delft, and F. B. Kugler, Real-frequency quantum field theory applied to the single-impurity Anderson model, Phys. Rev. B **109**, 115128 (2024).

[31] J. Kaye, K. Chen, and H. U. R. Strand, Comput. Phys. Commun. **280**, 108458 (2022).

[32] D. Kiese, H. U. R. Strand, K. Chen, N. Wentzell, O. Parcollet, and J. Kaye, Discrete Lehmann representation of three-point functions, arXiv:2405.06716.

[33] S. Dirnböck, S.-S. B. Lee, F. B. Kugler, S. Huber, J. von Delft, K. Held, and M. Wallerberger, Overcomplete intermediate representation of two-particle Green's functions and its relation to partial spectral functions, arXiv:2404.05541.

[34] M. Wallerberger, S. Badr, S. Hoshino, S. Huber, F. Kakizawa, T. Koretsune, Y. Nagai, K. Nogaki, T. Nomoto, H. Mori, J. Otsuki, S. Ozaki, T. Plaikner, R. Sakurai, C. Vogel, N. Witt, K. Yoshimi, and H. Shinaoka, SPARSE-IR: Optimal compression and sparse sampling of many-body propagators, SoftwareX **21**, 101266 (2023).

[35] H. Shinaoka, N. Chikano, E. Gull, J. Li, T. Nomoto, J. Otsuki, M. Wallerberger, T. Wang, and K. Yoshimi, Efficient *ab initio* many-body calculations based on sparse modeling of Matsubara Green's function, SciPost Phys. Lect. Notes, 63 (2022).

[36] H. Shinaoka and Y. Nagai, Sparse modeling of large-scale quantum impurity models with low symmetries, Phys. Rev. B **103**, 045120 (2021).

[37] J. Otsuki, M. Ohzeki, H. Shinaoka, and K. Yoshimi, Sparse modeling in quantum many-body problems, J. Phys. Soc. Jpn. **89**, 012001 (2020).

[38] L. Ying, Pole recovery from noisy data on imaginary axis, J. Sci. Comput. **92**, 107 (2022).

[39] L. Ying, Analytic continuation from limited noisy Matsubara data, J. Comput. Phys. **469**, 111549 (2022).

[40] J. Fei, C.-N. Yeh, and E. Gull, NEVANLINNA analytical continuation, Phys. Rev. Lett. **126**, 056402 (2021).

[41] K. Nogaki, J. Fei, E. Gull, and H. Shinaoka, NEVANLINNA.JL: A JULIA implementation of NEVANLINNA analytic continuation, SciPost Phys. Codebases, 19 (2023).

[42] K. Nogaki, J. Fei, E. Gull, and H. Shinaoka, Codebase release 1.0 for NEVANLINNA.JL, SciPost Phys. Codebases, 19-r1.0 (2023).

[43] S. Iskakov, C.-N. Yeh, P. Pokhilko, Y. Yu, L. Zhang, G. Harsha, V. Abraham, M. Wen, M. Wang, J. Adamski, T. Chen, E. Gull, and D. Zgid, Green/weak coupling: Implementation of fully self-consistent finite-temperature many-body perturbation theory for molecules and solids, arXiv:2406.18479.

[44] L. Zhang and E. Gull, Green-phys/pronyac: v0.1 (2024).

[45] L. Zhang and E. Gull, Green-phys/pronyac, https://github.com/Green-Phys/pronyac (2024).

[46] M. Wallerberger, H. Shinaoka, and A. Kauch, Solving the Bethe-Salpeter equation with exponential convergence, Phys. Rev. Res. **3**, 033168 (2021).

[47] H. Park, K. Haule, and G. Kotliar, Cluster dynamical mean field theory of the mott transition, Phys. Rev. Lett. **101**, 186403 (2008).

[48] F. Šimkovic, J. P. F. LeBlanc, A. J. Kim, Y. Deng, N. V. Prokof'ev, B. V. Svistunov, and E. Kozik, Extended crossover from a fermi liquid to a quasiantiferromagnet in the half-filled 2D Hubbard model, Phys. Rev. Lett. **124**, 017003 (2020).

[49] A. Georges, G. Kotliar, W. Krauth, and M. J. Rozenberg, Dynamical mean-field theory of strongly correlated fermion systems and the limit of infinite dimensions, Rev. Mod. Phys. **68**, 13 (1996).

[50] M. Eckstein, M. Kollar, K. Byczuk, and D. Vollhardt, Hopping on the Bethe lattice: Exact results for densities of states and dynamical mean-field theory, Phys. Rev. B **71**, 235119 (2005).

[51] O. Parcollet, M. Ferrero, T. Ayral, H. Hafermann, I. Krivenko, L. Messio, and P. Seth, Triqs: A toolbox for research on interacting quantum systems, Comput. Phys. Commun. **196**, 398 (2015).

[52] F. Gebhard, E. Jeckelmann, S. Mahlert, S. Nishimoto, and R. M. Noack, Fourth-order perturbation theory for the half-filled Hubbard model in infinite dimensions, Eur. Phys. J. B **36**, 491 (2003).

[53] N. Tsuji and P. Werner, Nonequilibrium dynamical mean-field theory based on weak-coupling perturbation expansions: Application to dynamical symmetry breaking in the Hubbard model, Phys. Rev. B **88**, 165115 (2013).

[54] A. Taheridehkordi, S. H. Curnoe, and J. P. F. LeBlanc, Optimal grouping of arbitrary diagrammatic expansions via analytic pole structure, Phys. Rev. B **101**, 125109 (2020).

[55] J. Kaye, Z. Huang, H. U. R. Strand, and D. Golež, Decomposing imaginary time Feynman diagrams using separable basis functions: Anderson impurity model strong coupling expansion, arXiv:2307.08566.

[56] T. A. Maier, M. Jarrell, T. Prushke, and M. Hettler, Quantum cluster theories, Rev. Mod. Phys. **77**, 1027 (2005).

[57] E. Gull, A. J. Millis, A. I. Lichtenstein, A. N. Rubtsov, M. Troyer, and P. Werner, Continuous-time Monte Carlo methods for quantum impurity models, Rev. Mod. Phys. **83**, 349 (2011).

[58] A. N. Rubtsov, M. I. Katsnelson, A. I. Lichtenstein, and A. Georges, Dual fermion approach to the two-dimensional Hubbard model: Antiferromagnetic fluctuations and fermi arcs, Phys. Rev. B **79**, 045133 (2009).

[59] J. P. F. LeBlanc, S. Li, X. Chen, R. Levy, A. E. Antipov, A. J. Millis, and E. Gull, Magnetic susceptibility and simulated neutron signal in the two-dimensional Hubbard model, Phys. Rev. B **100**, 075123 (2019).

[60] J. Kaufmann, C. Eckhardt, M. Pickem, M. Kitatani, A. Kauch, and K. Held, Self-consistent ladder dynamical vertex approximation, Phys. Rev. B **103**, 035120 (2021).

[61] M. Grandadam and J. P. F. LeBlanc, Planckian behaviour in the optical conductivity of the weakly coupled Hubbard model, arXiv:2303.04964.

[62] B. Michon, C. Berthod, C. W. Rischau, A. Ataei, L. Chen, S. Komiya, S. Ono, L. Taillefer, D. van der Marel, and A. Georges, Reconciling scaling of the optical conductivity of cuprate superconductors with Planckian resistivity and specific heat, Nat. Commun. **14**, 3033 (2023).

[63] J. J. Phillips and D. Zgid, Communication: The description of strong correlation within self-consistent Green's function second-order perturbation theory, J. Chem. Phys. **140**, 241101 (2014).

[64] O. J. Backhouse, M. Nusspickel, and G. H. Booth, Wave function perspective and efficient truncation of renormalized second-order perturbation theory, J. Chem. Theory Comput. **16**, 1090 (2020).

[65] C. J. C. Scott, O. J. Backhouse, and G. H. Booth, A moment-conserving reformulation of GW theory, J. Chem. Phys. **158**, 124102 (2023).

[66] P. Pokhilko, C.-N. Yeh, M. A. Morales, and D. Zgid, Tensor hypercontraction for fully self-consistent imaginary-time GF2 and gwsox methods: Theory, implementation, and role of the Green's function second-order exchange for intermolecular interactions, arXiv:2404.17744.

[67] M. K. Ritter, D. Kiese, T. Müller, F. B. Kugler, R. Thomale, S. Trebst, and J. von Delft, Benchmark calculations of multiloop pseudofermion FRG, Eur. Phys. J. B **95**, 102 (2022).

[68] H. Shinaoka, J. Otsuki, M. Ohzeki, and K. Yoshimi, Compressing Green's function using intermediate representation between imaginary-time and real-frequency domains, Phys. Rev. B **96**, 035147 (2017).

[69] J. Li, M. Wallerberger, N. Chikano, C.-N. Yeh, E. Gull, and H. Shinaoka, Sparse sampling approach to efficient *ab initio* calculations at finite temperature, Phys. Rev. B **101**, 035144 (2020).